Natanael Suwandi[1], Fei Jiang[2,3], Takeshi Tsuji[1,2,4]

[1]Department of Cooperative Program for Resources Engineering, Graduate School of Engineering, Kyushu University, Fukuoka 819-0395, Japan

[2]International Institute for Carbon-Neutral Energy Research, Kyushu University, Fukuoka 819-0395, Japan

[3]Department of Mechanical Engineering, Graduate School of Sciences and Technology for Innovation, Yamaguchi University, Yamaguchi 755-8611, Japan

[4]Department of Earth Resources Engineering, Faculty of Engineering, Kyushu University, Fukuoka 819-0395, Japan

Corresponding author: Takeshi Tsuji (tsuji@mine.kyushu-u.ac.jp)

Key Points:

- Relative permeability in two-phase flow is calculated in a three-dimensional digital Berea rock using Lattice Boltzmann Method

- Relative permeability varies due to lubrication effect, shear drag force effect, and capillary force, and is related to fluid connectivity

- Relative permeability on viscosity ratio-capillary number diagram is created to predict spatiotemporal variation of reservoir permeability

Abstract

The relative roles of parameters governing relative permeability, a crucial property for two-phase fluid flows, are imperfectly known. To characterize the influence of viscosity ratio (M) and capillary number (Ca), we calculated relative permeabilities of nonwetting fluids (k_{nw}) and wetting fluids (k_w) in a 3D model of Berea sandstone using the lattice Boltzmann method. We applied the Euler–Poincaré characteristic to quantify the morphology of both fluids. We show that k_{nw} increases and k_w decreases as M increases due to the lubricating effect and instability at fluid interfaces resulting from viscosity contrast. We also show that k_{nw} decreases markedly at low Ca ($\log Ca < -1.25$), whereas k_w undergoes negligible change with changing Ca. An M–Ca–k_{nw} correlation diagram, displaying the simultaneous effects of M and Ca, shows that they cause k_{nw} to vary by an order of magnitude, an effect not incorporated in current estimation techniques.

Plain Language Summary

The relative permeability is a crucial parameter in a system where two fluid phases exist simultaneously. For example, in carbon capture and storage, relative permeability is important to assess the replacement mechanism of the existing fluid in the reservoir (wetting fluid) by the injected CO_2 (non-wetting fluid). It is also an important parameter in enhanced oil recovery fields, as high relative permeability of oil indicates that the oil in the reservoir can be extracted quickly. The relative permeability is temporally and spatially varied

1

by reservoir conditions (e.g., temperature). But currently, in reservoir-scale fluid flow simulation, relative permeability is assumed to be constant regardless of the different conditions. In this study, we conducted simulations to calculate relative permeability in various viscosity ratio (M) and capillary number (Ca) conditions. We found that relative permeability changes dramatically in different M and Ca conditions, and we further mapped relative permeability on the diagram between M and Ca to predict relative permeability accurately in various reservoir conditions. Our findings can be useful to determine the suitable fluid properties to be used in reservoir management and to accurately estimate fluid behavior based on reservoir-scale simulation with variant relative permeability.

1 Introduction

The relative permeability of the different fluids in a two-phase flow has been a lively area of study in scientific and engineering fields concerned with two-phase flows in geological reservoirs, such as in carbon capture and storage (CCS) fields, enhanced oil recovery (EOR) operations, geothermal power systems, and geological radioactive waste disposal repositories (Benson et al., 2015; C. Chen & Zhang, 2010; Gudjonsdottir et al., 2015; Niibori et al., 2011; Shad et al., 2008; Wu & Wang, 2020). Relative permeability is a crucial hydraulic property for modeling the flow of both fluids and assessing the mechanisms of fluid displacement in the reservoir. For example, when CO_2 is injected into a CCS reservoir, the CO_2 (nonwetting phase) displaces the existing fluid in the reservoir, such as oil or brine (wetting phase). Relative permeability values can be used to estimate the reduction in CO_2 fluid flow due to surface-tension effects between CO_2 and the brine, thus the parameter is useful to assess the injectivity of the CO_2 (Benson et al., 2015; Burnside & Naylor, 2014). The relative permeability can also aid estimation of how much fluid can be displaced by CO_2 before the system reaches the wetting fluid irreducible saturation condition, limiting the CO_2 volume that can be stored in the reservoir (Burnside & Naylor, 2014). Conversely, in EOR systems the best results are obtained when the relative permeability is high for oil and low for the injected fluid (Heins et al., 2014).

In a two-phase flow system, the interaction between the two fluids is vital in determining the relative permeability of each fluid. Therefore, the relative permeability value of each fluid is not only a function of saturation, but is also affected by other parameters related to its interaction with the other fluid component. Lenormand et al. (1988) reported that two parameters, viscosity ratio and capillary number, can explain the interaction between two immiscible fluids. The viscosity ratio (M) is a dimensionless parameter describing the ratio between the viscosity of the injected nonwetting fluid and the viscosity of the ambient wetting fluid:

$$M = \frac{\mu_{\text{nw}}}{\mu_w} \qquad (1)$$

where μ_{nw} is the dynamic viscosity of the nonwetting fluid and μ_w is the dynamic viscosity of the wetting fluid.

The capillary number (Ca) is a dimensionless parameter describing the ratio between the viscous drag forces and the interfacial tension forces between two immiscible fluids:

$$Ca = \frac{\mu_{nw} V_{nw}}{\sigma} \qquad (2)$$

where V_{nw} is the average fluid velocity of the nonwetting fluid and σ is the interfacial tension (IFT) between the two fluids.

Despite the recognition that the relative permeability k is a function of M, several studies of this relationship have reported divergent results. An experimental study (Odeh, 1959) found that the relative permeability of the nonwetting fluid (k_{nw}) increases and the relative permeability of the wetting fluid (k_w) stays relatively constant as M increases, as have several other experimental and numerical studies (Dou & Zhou, 2013; Goldsmith & Mason, 1963; Huang & Lu, 2009; Jeong et al., 2017; Mahmoudi et al., 2017; Yiotis et al., 2007; Zhao et al., 2017). An analytical study of co-current annular flow in which the wetting fluid is distributed on the pore surface and the nonwetting fluid is in the middle of the pore produced empirical equations for the nonwetting and wetting fluids as a function of M and saturation:

$$k_{nw} = S_{nw} \left[\frac{3}{2}M + S_{nw}{}^2 (1 - \frac{3}{2}M) \right] \qquad (3)$$

$$k_w = \frac{1}{2}(1 - S_w)^2 (3 - S_w) \qquad (4)$$

where S_{nw} is the saturation of the nonwetting fluid, and $S_w = 1 - S_{nw}$ is the saturation of the wetting fluid. These equations suggest that k_w is not affected by increasing M and is a function of saturation alone. However, other studies have reported that k_{nw} increases and k_w decreases as M increases (Ahmadlouydarab et al., 2012; Fan et al., 2019; Goel et al., 2016; Ramstad et al., 2010); thus, there is as yet no general agreement on the variation of k_w with increasing M. One of the challenges of previous studies was the difficulty of removing the effects of capillary forces and wettability factors when evaluating this relationship.

Similarly, studies of the influence of Ca on relative permeability is still imperfectly known. An experimental study (Fulcher et al., 1985) concluded that ks_{nw} is a function of IFT rather than Ca, such that k_{nw} increases as IFT decreases (Ca increases), and that k_w consistently increases as Ca increases, but not as much as k_{nw} increases, as IFT decreases. Several studies (Asar & Handy, 1989; Fan et al., 2019; Harbert, 1983) also found that k_{nw} and k_w increase as IFT decreases because the two fluids interfere less with each other and thus tend to

3

form more well-connected flow pathways. One of the studies (Asar & Handy, 1989) showed that both fluids relative permeability curves tend to straighten and approach the 45° tangent line as IFT approaches zero. Other studies (Amaefule & Handy, 1982; Jiang et al., 2014; Shen et al., 2010) also concluded that both k_{nw} and k_w decrease as Ca decreases. On the other hand, a numerical study (Zhao et al., 2017) concluded that k_w increases with increasing Ca under neutral wetting conditions (= 90°) but stays relatively constant with increasing Ca under strong wetting conditions (= 135°). These divergent results warrant further investigations of how relative permeability changes with changing IFT and Ca. One of the challenges in this evaluation is the difficulty of isolating the effect of IFT while keeping other parameters, such as viscosity, constant. Thus, it is difficult to hold Ca constant in all simulation conditions.

Previous studies have usually evaluated the separate effects of M and Ca on relative permeability. However, in two-phase flows, the effects of viscosity gradient and interfacial tension must be evaluated simultaneously to accurately predict the relative permeability in the system. Because few studies have evaluated the condition when both parameters influence relative permeability using a steady-state simulation, our aim in this work was to fill that knowledge gap.

In this paper, we clarify the effects of viscosity ratio and capillary number on the relative permeability of nonwetting and wetting fluids from the results of a color gradient lattice Boltzmann method (LBM) simulation using a three-dimensional (3D) digital rock. We begin by evaluating the effects of the two parameters individually by holding other parameters constant. We use the Euler–Poincaré characteristic or Euler number to describe the fluid connectedness, a factor that is directly related to relative permeability. We then map k_{nw} in various M–Ca conditions in search of general trends. By understanding the variations of relative permeability in the M–Ca parameter space, we can conduct accurate large-scale reservoir simulations by considering the reservoir conditions M and Ca and thereby contribute to the wide range of research regarding applications that employ two-phase fluid mixtures.

2 Methods

2.1 Lattice Boltzmann Method

The LBM is a branch of computational fluid dynamics that has emerged as a popular technique to solve multiphase fluid flow systems in complex geometries because of its algorithmic simplicity (S. Chen & Doolen, 1998; Dou & Zhou, 2013; Jiang et al., 2014; Ramstad et al., 2010; Succi et al., 2010). LBM simulations treat fluids as a group consisting of fictive particles; the movement of these particles is simulated with a statistical approach. The movement of the bulk fluid is simulated from propagation and collision processes of the fictive particles (Huang et al., 2011). We chose the Rothman–Keller color gradient model (Tölke et al., 2006) to conduct the simulations because it can simulate a high fluid viscosity ratio with better accuracy than other LBM models (Ahrenholz et al., 2008; Yang & Boek, 2013). The color gradient model is so named

4

because it graphically represents two-phase fluids as a mixture of a wetting and nonwetting fluid, assigned the colors blue and red, respectively (Huang et al., 2015). Our 3D simulations used the D3Q19 (3 dimensions, 19 velocity lattice) velocity model.
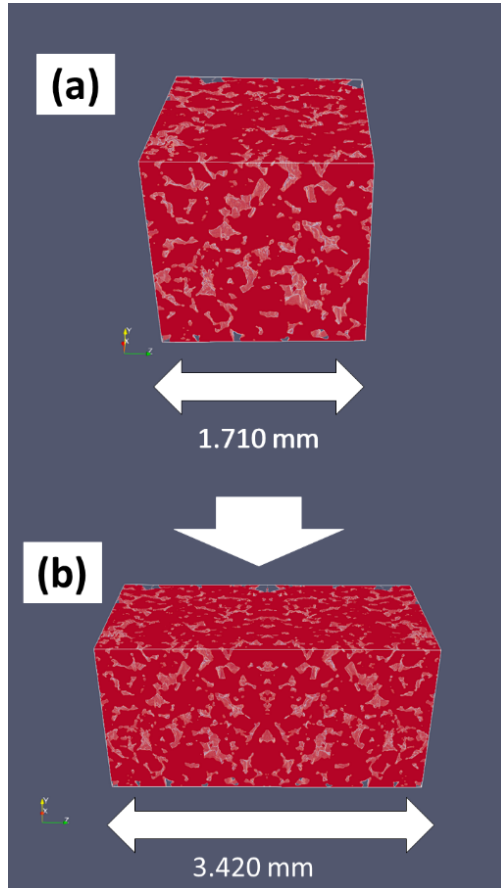
2.2 Digital rock model

We used a 3D digital rock model obtained from microtomographic images of Berea sandstone (Fig. 1a). Berea sandstone is chosen due to its relatively well-known properties (Øren & Bakke, 2003). The rock has a relatively large mean grain size of 250 m and consists of quartz, feldspar, carbonates, and clay minerals. Its average pore size is 20 m with a relatively high size deviation (Jiang & Tsuji, 2015). The simulation requires a rock model that is larger than its representative elementary volume (1 mm for Berea sandstone), and the multi-pore nature of the rock must be considered. Our rock model, obtained from the database of Dong and Blunt (2009), is a stack of 320 tomographic images, each one measuring 320×320 pixels. The resolution of the image is 5.345 µm; thus, the digital rock represents an actual size of $1.710 \times 1.710 \times$

1.710 mm.

2.3 Relative permeability calculation

The viscosity ratio M is defined by dividing the nonwetting fluid's viscosity (μ_{nw}) by the wetting fluid's viscosity (μ_w) (equation 1). In the LBM, μ can be calculated as follows:

$$\mu \; = \; \frac{1}{3}(\tau \; - \; \frac{1}{2}) \qquad (5)$$

where τ represents the relaxation parameter. Thus, the viscosities of both fluids can be modified by changing the τ value. Because τ must be larger than 0.5 for a positive viscosity and the simulation becomes unstable as τ approaches 0.5, it is important that the simulation uses a τ value that ensures its stability and accuracy. In this study, we altered M only by changing the τ value of the nonwetting fluid to manipulate μ_{nw} and keeping μ_w constant throughout the simulation to preserve its stability.

The capillary number Ca can be modified based on equation (2) by changing the μ and μ_{nw} parameters. Because μ_{nw} is also used to determine M, we achieved the desired Ca by adjusting μ alone. The average velocity of the nonwetting fluid phase after the simulation has converged to equilibrium, defined as a change less than log $Ca = \pm 0.1$, was used to calculate the Ca number. When the fluid velocity change in the last 1,000 simulation steps was less than 2% for all cases, the simulations were assumed to have converged at that time. The time-averaged Ca value in the last 3,000 steps was calculated for further investigation.

To remove the complications arising from wettability effects, we assumed that the solid was completely nonwetting ($\theta = 180°$) in all conditions. Given that condition, the wetting fluid fills small pore spaces and completely coats the surface of the rock, whereas the nonwetting fluid is not in contact with the pore wall and can only occupy the central parts of large pores.

We applied a steady-state simulation condition, which assumes that the wetting fluid saturation (S_w) and nonwetting fluid saturation (S_{nw}) are kept constant. In the initial state, both fluids were specified as being randomly distributed in the pore spaces. This initial condition was chosen because the initial fluid connectivity is reduced, which can lead to increased capillary trapping (Jiang & Tsuji, 2016). This initial condition is desirable in a CCS site to increase the residual CO_2 saturation. Periodic boundary conditions were applied in the x, y, and z directions of our 3D model. A constant body force was applied in z direction to both fluids to mimic the pressure gradient: $g = dP/dz$. For the interaction between rock solid nodes and fluid voxels, no-slip boundary conditions were applied using the halfway bounce back scheme. The density of both fluids was set at 1.0 in lattice units, which corresponds to 1,000 kg/m^3 in the physical unit. We did this because our study was focused on viscosity differences, and the effect of density contrast is minor if inertial force can be neglected.

We applied a periodic boundary condition in the flow direction; therefore, the rock was mirrored in the z direction to ensure that the pore spaces on the right side were connected to the left side of the digital rock (Fig. 1b).

2.3.1 Relative permeability curve

The relative permeability curve is a plot of k versus saturation S. As S_{nw} increases, k_{nw} increases and k_w decreases. The shape of this curve can change as a result of viscous drag force and capillary force; thus, an investigation of its variation with changes in M and Ca is important to determine the optimum conditions to achieve the desired value of k. We plotted k_{nw} and k_w as a function of S_{nw} to create relative permeability curves for various conditions.

In this study, the wetting fluid viscosity was kept constant at 0.15 in lattice units in all simulations, and M was manipulated by altering only $_{nw}$. Changes in M can be interpreted as a change in either $_w$ or $_{nw}$; thus, modifying either viscosity value will produce the same results if their ratio is maintained.

It must also be noted that, because we conducted a steady-state simulation, the S_{nw} value used for plotting the permeability curve might be unrealistic in actual injection settings. Previous research has shown that the maximum S_{nw} or irreducible S_w depends on M and Ca (Tsuji et al., 2016). For instance, at low Ca and low M conditions, the maximum S_{nw} can be less than 50%. However, for the sake of consistency, in this study we plotted all permeability curves for S_{nw} values of 10% to 90%.

2.3.2 M–Ca–permeability color map

After confirming the influence of M and Ca on k_{nw} and k_w in a two-phase flow system, we conducted simulations at various M and Ca conditions with S_{nw} held at a constant value of 20% to create a plot of M–Ca–k_{nw} correlation or color diagram. The 20% S_{nw} condition was chosen because it can realistically be achieved under all M–Ca conditions (Tsuji et al., 2016). The color diagram is useful to evaluate the degree of influence of M and Ca on changes of relative permeability when both parameters influence a system, and can also provide estimates of relative permeability in a reservoir under a wide range of M and Ca.

3 Results and interpretation

Before conducting simulations in various M and Ca conditions, we first ran single-phase simulations to determine the absolute permeability value of the porous media and to verify the stability of the simulation. The results are presented in Appendix A. The effects of M and Ca were then evaluated individually to see how they influence nonwetting and wetting relative permeability curves in a two-phase flow system. Next, we conducted simulations over a wide range of M and Ca values at a S_{nw} value of 20% to create a relative permeability color diagram.

3.1 Relative permeability curve from a two-phase simulation

(a) Nonwetting fluid relative permeability

(b) Wetting fluid relative permeability
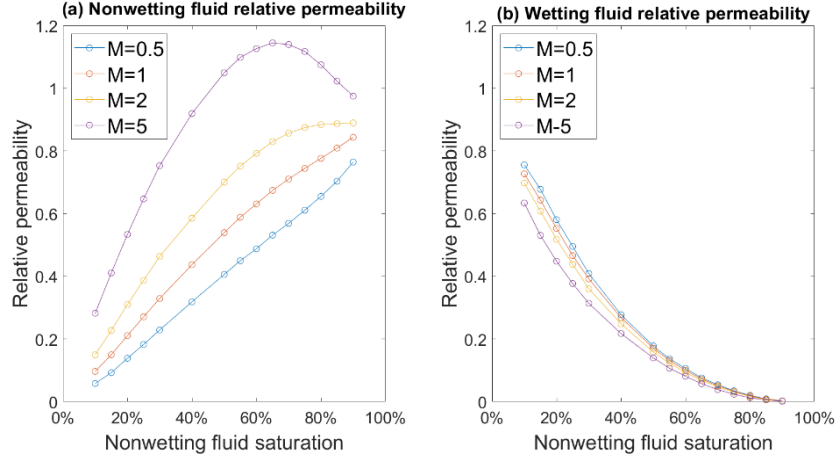
3.1.1 Effect of changes in M on k_{nw} and k_w

We plotted values of k_{nw} for four values of M (5, 2, 1, and 0.5) over the full realistic range of S_{nw} (10% to 90%) while holding log Ca nearly constant at -0.25 ± 0.1 (Fig. 2a). The k_{nw} value increases as M increases, especially for intermediate S_{nw} values (30% to 70%). For $M = 5$, k_{nw} exceeds 1 in some S_{nw} conditions; that is, it exceeds the intrinsic permeability of the rock. This result agrees with previous studies and can be explained by the lubrication effect, also known as the viscous coupling effect (Goel et al., 2016; Li et al., 2005; Ramstad et al., 2010; Yiotis et al., 2007; Zhao et al., 2017).
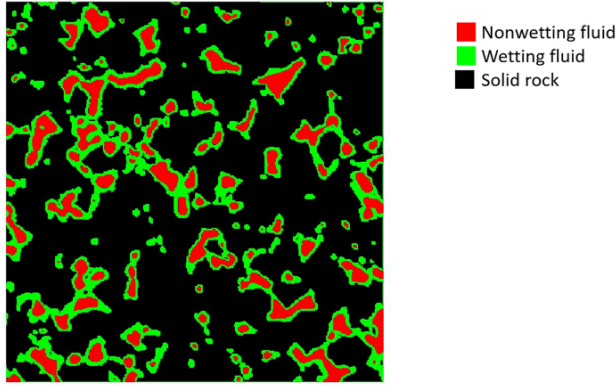
To illustrate the lubrication effect, we provide a 2D image showing the distribution of nonwetting fluid, wetting fluid, and solid rock at the final state of the simulation with S_{nw} =50%, $M = 5$, and log Ca of -0.25 (Fig. 3). Because the wetting fluid layer is always present between the nonwetting fluid and the rock, the wetting fluid moves along the rock surface and the nonwetting phase is confined to the central part of the pore. Thus, the velocity of the nonwetting fluid is affected only by the momentum transfer across fluid–fluid interfaces and

not by contact with the pore wall.

At sufficiently high values of M, the wetting fluid acts as a lubricant that enhances the movement of the nonwetting fluid, making its permeability higher than in the single-phase condition such that k_{nw} is greater than 1 (Fig. 2a). This lubrication effect most strongly affects k_{nw} in the intermediate S_{nw} range, when the wetting fluid forms thick films that provide the nonwetting fluid with a moving boundary (Vafai, 2000). At low S_{nw}, the nonwetting phase tends to form droplets with low connectivity; thus, the lubrication effect is less pronounced. At high S_{nw}, k_{nw} also decreases toward unity because less wetting fluid is present in the rock and the nonwetting phase comes into contact with the rock, degrading the lubrication effect and reducing k_{nw} near to the single-phase condition. Because the lubrication effect occurs at high M values, it is commonly observed in mixtures of heavy oil and water in EOR systems and has been confirmed by experimental results (Goel et al., 2016; Shad et al., 2008).

Our results demonstrate that k_w decreases as M increases (Fig. 2b). This phenomenon can be attributed to the increase of shear drag force from the nonwetting phase. As M increases, the viscosity of the nonwetting fluid increases, which inhibits the flow of the wetting fluid such that it has a lower k_w.
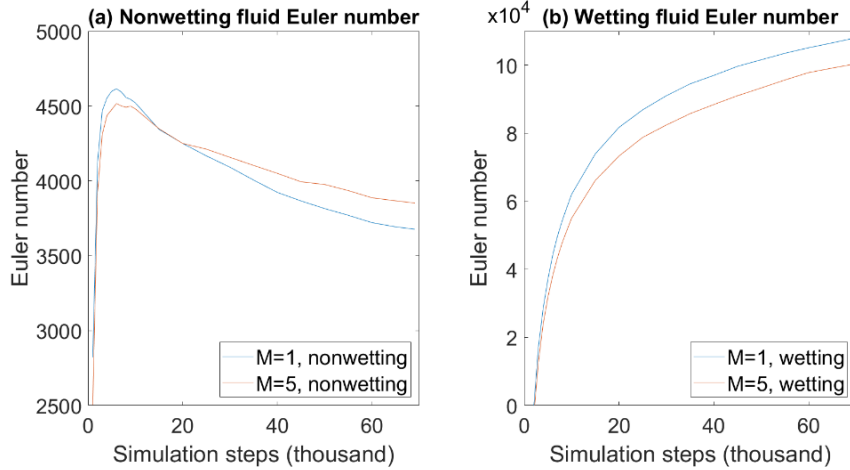
To investigate the connectivity of each fluid phase, we calculated the Euler–Poincaré characteristic (Euler number hereafter). Euler number has been used to investigate the effect of pore space heterogeneity on permeability and the effect of fluid saturation on the fluid connectivity (Schlüter et al., 2016; Zhang et al., 2022) and the morphology of the nonwetting and wetting fluids is predicted to have a great influence on the relative permeability. The method to calculate Euler number in this study is described in Appendix B.

We considered the evolution of the Euler number for the nonwetting fluid during simulations with $M = 1$ and $M = 5$, $\log Ca = -0.25 \pm 0.1$, and S_{nw} of 50% (Fig. 4a). In the first 10,000 steps, the Euler number in both simulation conditions

increases, which indicates that at this time, the nonwetting fluid is unstable and keeps forming new fluid clusters. After 10,000 steps, the Euler number for both simulation conditions starts to decrease, suggesting that some of the nonwetting fluid clusters become more connected and form larger clusters as the simulation proceeds. In the final converged condition, the Euler number is higher for $M = 5$ than for $M = 1$. This result indicates that at $M = 5$, the nonwetting fluid forms more individual clusters and has less fluid connectivity than at $M = 1$. This difference is the result of the instability of the interface of the fluids due to the viscosity stratification (Yiantsios & Higgins, 1988; Yih, 1967). When two immiscible fluids have different viscosities, their velocities will also be different at their interface, causing instability. The instability causes the nonwetting fluid to create more clusters, decreasing its fluid connectivity. In addition, as more clusters are formed, the size of the nonwetting fluid clusters is smaller, and it is easier for them to pass through the pore space. At $M = 1$, the nonwetting fluid is more connected and its fluid clusters are larger. The larger clusters cannot pass through the small pore throats, leading to lower k_{nw}.

We also calculated the evolution of the Euler number for the wetting fluid under the same M and Ca conditions (Fig. 4b). For both $M = 1$ and $M = 5$, the Euler number keeps increasing during the simulation, which indicates that the wetting fluid keeps getting more disconnected before convergence. The Euler number for $M = 1$ is higher than the Euler number for $M = 5$, because larger number of nonwetting fluid clusters are formed at M=5 compared to at M=1. This also indicates that wetting fluid has higher connectivity at $M = 5$ and therefore has a larger area of contact with the solid and receives more drag force; thus, k_w is lower at $M = 5$ than at $M = 1$.

To confirm our interpretation, we also calculated the degree of contact between the wetting fluid and the solid wall for $M = 1$ and $M = 5$, as indicated by the number of wetting fluid voxels attached to the solid surface. At the start of the simulation, 47.38 % and 47.57 % of wetting fluid voxels were attached to the solid surface at $M = 1$ and $M = 5$, respectively. When the simulations converged, these respective numbers were 81.17 % and 82.58 %. This result confirms that, at $M = 5$, the wetting phase fluid is more strongly attached to the solid wall and receives more drag force from the solid wall, thus the k_w is lower at $M = 5$ than at $M = 1$, as shown in Fig. 2b.
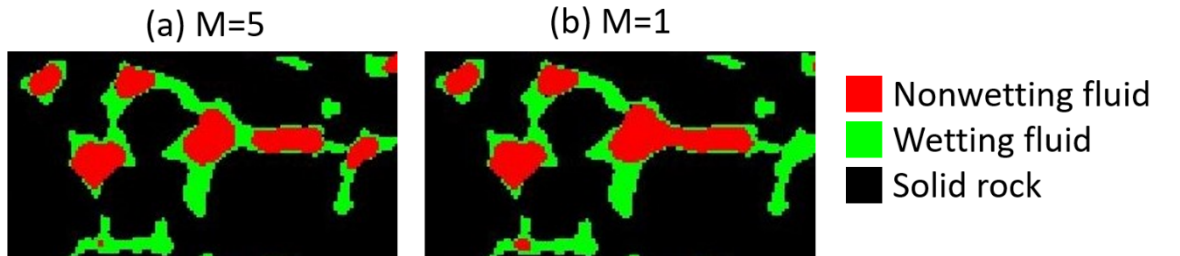
To obtain further insights into fluid cluster size and connectivity, we considered

the distribution of nonwetting and wetting fluids in one section of a 2D slice of the simulated specimen for $M = 1$ and $M = 5$ at log Ca $= -0.25 \pm 0.1$ and 50% saturation after the simulation had converged (Fig. 5). The nonwetting fluid (red) at M=5 forms small, unconnected clusters in the pore throats, while at M=1, the nonwetting fluid forms a large, connected cluster in the pore throat. Thus, the nonwetting fluid clusters are larger and more connected at $M = 1$ than at $M = 5$. Due to the increase of number of nonwetting fluid clusters, the wetting fluid (green) at M=5 has more contact area with the rock surface compared to M=1, thus the wetting fluid receives more drag force from the rock and causes decrease in relative permeability.
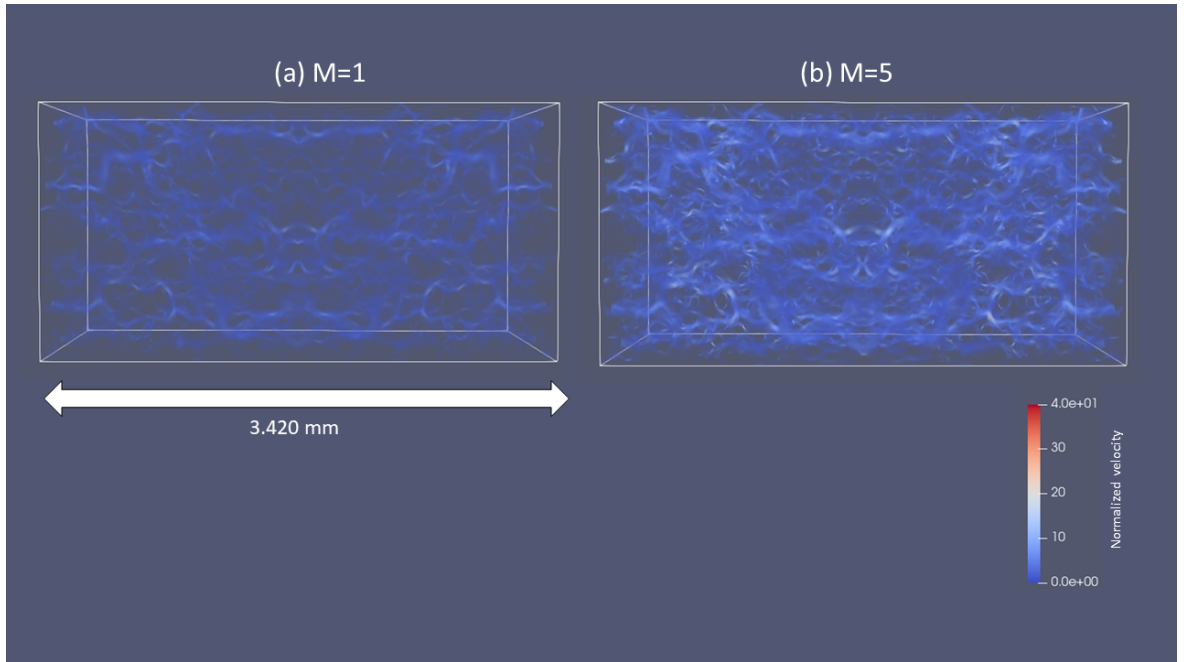
The results of normalized fluid velocity distribution for M=1 and M=5 in the pore spaces at 50% saturation after the simulation converges are plotted in Figs. 6a and 6b, respectively. The fluid velocity field is normalized to consider the effect of viscosity change using the equation $U^* = \frac{U}{PL/\mu}$. It can be seen that the normalized fluid velocity is higher at $M = 5$ than at $M = 1$, indicating that k_{nw} is higher at $M = 5$ than at $M = 1$, in agreement with our relative permeability curve.
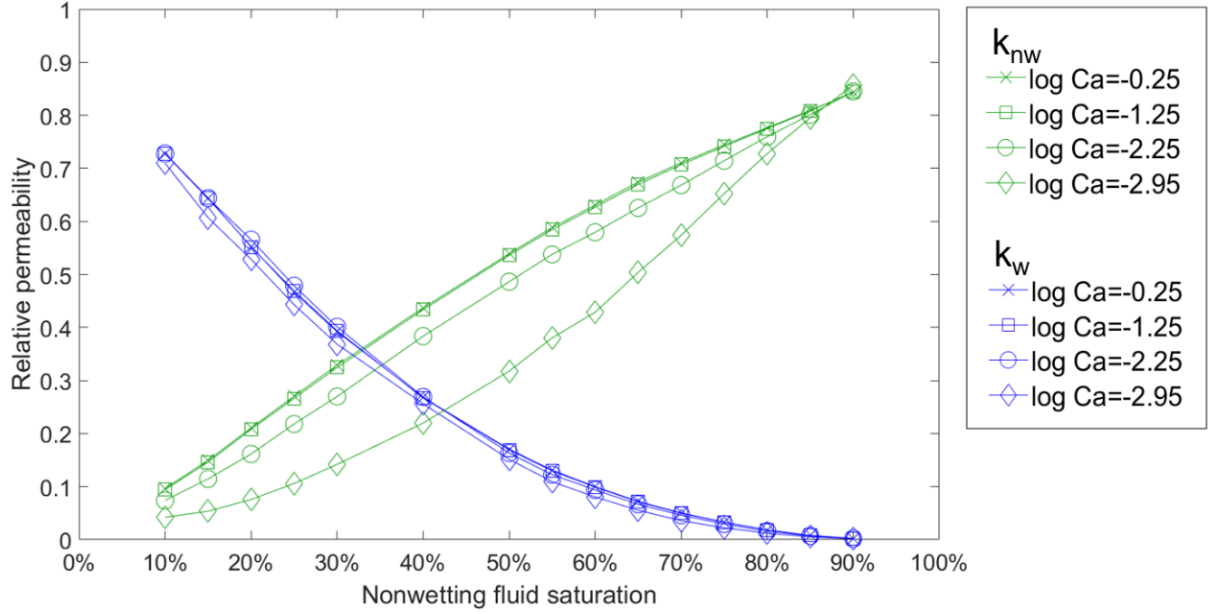
3.1.2 Effect of Ca change on k_{nw} and k_{w}

The k_{nw} and k_{w} curves for four different values of log Ca at $M = 1$ (-0.25, -1.25, -2.25, and -2.95) are plotted in Fig. 7. The Ca value is altered by changing the IFT value. The k_{nw} values remain relatively constant between log $Ca = -0.25$ and -1.25, i.e., for high Ca/low IFT values, and the relative permeability curve for the nonwetting fluid is an approximately straight line, in agreement with previous studies (Asar & Handy, 1989; Shen et al., 2010). However, as log Ca becomes lower than -1.25, k_{nw} notably decreases. This decrease occurs because the flow of the nonwetting fluid is more strongly inhibited by capillary force when Ca is low. Capillary force is controlled by IFT, the surface tension forces between the nonwetting and wetting fluids. As IFT increases, the nonwetting fluid becomes trapped by the larger capillary force in the small pore spaces, thus causing k_{nw} to decrease. As Ca becomes lower, the influence of capillary force becomes more dominant. The result suggests that k_{nw} does not decrease linearly with changes in IFT/Ca.

For the wetting fluid, k_{w} also decreases as Ca decreases (Fig. 7), but at a much smaller rate compared to k_{nw}, consistent with previous research (Harbert, 1983; Jiang et al., 2014; McDougall et al., 2007; Ramstad et al., 2010; Zhao et al., 2017). The reason is that as shown in Fig. 3, in our simulation, the wetting fluid only flows along the rock surface and the nonwetting fluid flows in the central part of the pores. Thus, the wetting fluid is mainly affected by interaction with the rock surface, and the change in capillary force has a negligible effect. We conclude that the variation in k_{w} is dominated by the fluid saturation in the system and is little affected by changes in IFT or Ca.

3.2 M–Ca–k_{nw} color diagram

After confirming the influence of M and Ca on k_{nw} and k_w in a two-phase flow system, we conducted simulations with various values of M and Ca at a constant 20% S_{nw} value to create an M–Ca–k_{nw} correlation diagram. We chose the 20% S_{nw} condition because it is realistic under all M–Ca conditions (Tsuji et al., 2016). We created the color diagram only for the nonwetting fluid because the relative permeability curves (Fig. 7) demonstrate that k_w does not respond markedly to changes in Ca.

Color maps are useful to provide estimates of k_{nw} under a wide range of M and Ca conditions in a reservoir and to analyze the degree of influence on k_{nw} by M and Ca. Two color maps are presented in Fig. 8. The first color map (Fig. 8a) depicts the parameter space of $\log M = -0.70$ to 0.70 and $\log Ca = -3.00$ to -0.50, which represents the broad range of conditions relevant to reservoirs. Values higher than this range are hard to achieve at the field scale, and lower values are outside the stable range of the simulation. The second color map (Fig. 8b), covering the lower left quadrant of the parameter range shown in Fig. 8a, was produced to increase the accuracy of k_{nw} estimates for a system with low M and low Ca, which is common in the CCS field (Zheng et al., 2017).
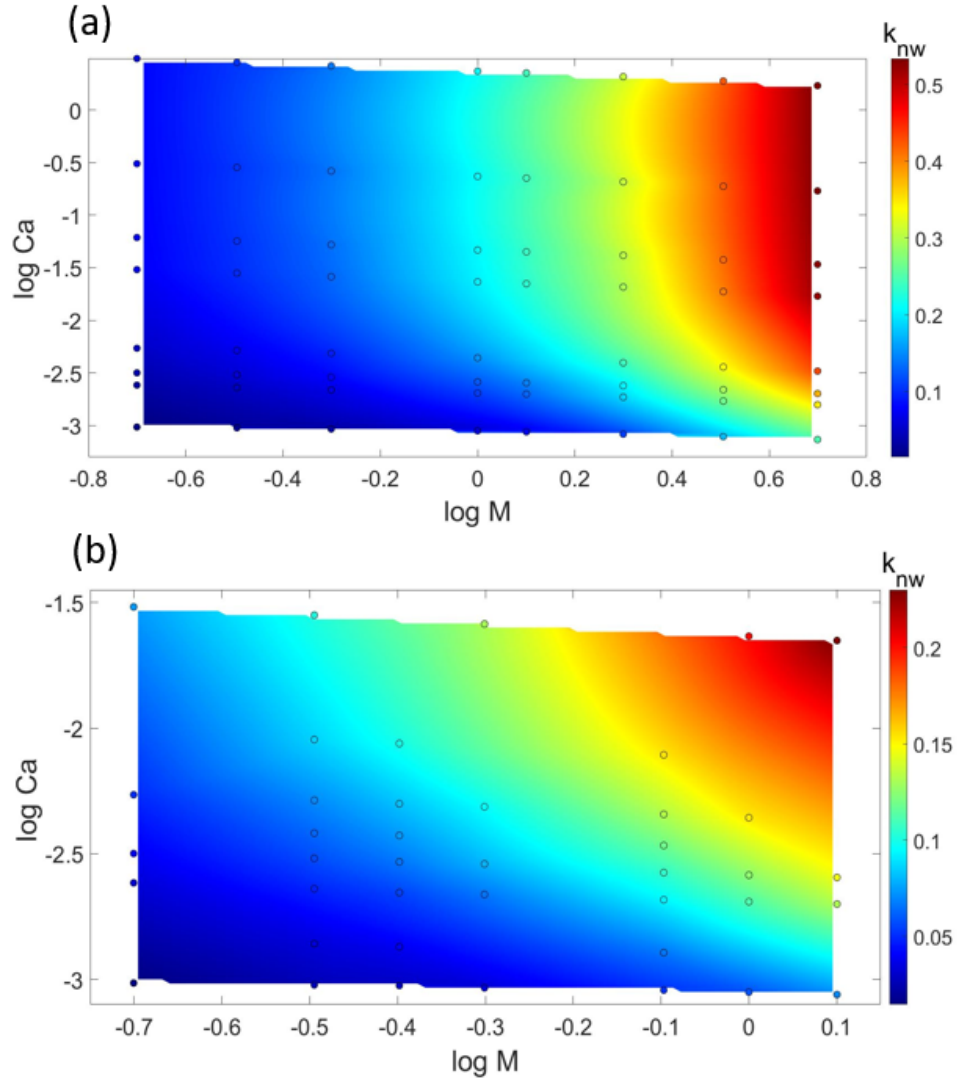
In the specified parameter range, k_{nw} varies from 0.02 to 0.54 (Fig. 8a). For high log Ca values (between -1.25 and $+0.5$), k_{nw} does not vary with log Ca and is only influenced by M, as indicated by the almost straight vertical borders between color bands. This finding agrees with Fig. 7, which shows that for log Ca -1.25, the nonwetting fluid relative permeability curve is not affected by Ca. However, as log Ca becomes lower than -1.25 (Ca value 0.06), k_{nw} can be seen to vary on both the x axis (log M) and the y axis (log Ca), that is, k_{nw} starts to be affected by the capillary force. The diagram agrees with our finding in section 3.2 that for log Ca lower than -1.25, k_{nw} decreases as Ca decreases.

The k_{nw} variation with M (x axis) is more pronounced for $\log M > 0$ ($M > 1$) than for $\log M < 0$ (Fig. 8a). This result is consistent with our findings in section 3.1 and is caused by the lubrication effect resulting from viscosity differences. When $_{nw}$ is higher than $_{w}$, the resulting instability and viscous coupling effect enhances the relative permeability of the nonwetting fluid. The diagram clearly captures the contrast between k_{nw} at $\log M < 0$ and at $\log M > 0$.

The range of k_{nw} variation in low M and low Ca conditions is obvious in the magnified part of the diagram (Fig. 8b). The range of k_{nw} values is 0.02 to 0.25, in a part of parameter space where both Ca and M influence k_{nw} and thus the borders between color bands are curved. The diagram is useful for evaluating k_{nw} when the effects of viscosity gradient and capillary number are considered simultaneously, and the graph neatly summarizes all the main results of this study. The diagram shows that capillary force starts affecting the flow of the nonwetting fluid when $\log Ca$ is less than -1.25 and that the effect of changes in capillary number may be just as important as that of changes in viscosity ratio. The graph also shows that k_{nw} is affected by M under all conditions, but most markedly when $\log M > 0$. The graph yields a good estimate of k_{nw} at 20% saturation based on the M and Ca parameters.

4 Discussion

We have demonstrated how M and Ca can markedly change the relative permeabilities of the nonwetting and wetting fluids in a reservoir; thus, our results can help identify the optimum properties of the immiscible fluids to be used in a geologic reservoir. For example, in a CCS project, the injectivity of the CO_2 is highest when the reservoir fluid has a lower viscosity and the IFT between the two fluids is low. Thus, the relative permeability of injected CO_2 is higher in a saline aquifer than in an oil field. For an EOR project, the relative permeability of oil is higher when a fluid with low viscosity is injected.

The relative permeability map (Fig. 8) is useful to provide accurate estimates of k_{nw} in reservoir-scale simulations. Currently, the relative permeabilities of the nonwetting and wetting fluid are simulated on the basis of a uniform relative permeability curve, without regard to the M and Ca conditions. However, we have shown that the nonwetting fluid, at a typical saturation (S_{nw}) of 20%, can vary in relative permeability by an order of magnitude, from 0.02 to 0.54, depending on M and Ca conditions. The color map created in this study can provide more accurate estimates of relative permeability (e.g., temporal permeability variations in a 3D reservoir model) if Ca and M are derived from the reservoir simulation. In addition, although the M generally remains constant in the two-phase flow, the Ca value can greatly changes depending on the distance from the injection well in a reservoir. For example, when evaluating the reservoir area located near the injection well, the injection pressure creates a high-pressure gradient which causes the injected fluid velocity to be high. As the fluid flows away from the injection site, the fluid velocity becomes slower, thus the k_{nw} becomes lower. This means that fluid relative permeability varies

based on location inside the reservoir, and the permeability variation can be evaluated using the relative permeability map, thus providing a more accurate relative permeability estimation.

In this study, we created a relative permeability map for $S_{nw} = 20\%$, which is a reasonable condition that can be achieved in all or most systems. As S_{nw} increases, k_{nw} also increases until it reaches its maximum value (e.g., k_{nw} at the irreducible saturation). Therefore, it is advisable to create relative permeability maps for several saturation conditions. One possible future direction from this study would be to create a four-dimensional M–Ca–S_{nw}–k_{nw} graph to yield k_{nw} estimates for all saturation conditions. Nevertheless, the great consistency of variations in k caused by changes in M and Ca found in this study suggests that maps for other saturation conditions will have similar features to Fig. 8.

In this study, we produced a relative permeability diagram for a digital specimen of Berea sandstone. In addition to M and Ca, the influences upon relative permeability include the pore geometry of the rock, such as pore size distribution, pore connectivity, and other parameters. These parameters differ among rock formations, meaning that the relative permeability maps of different types of reservoir rocks will vary. Our methodology makes it possible to create accurate maps of relative permeability for other reservoir rocks.

In geological CO_2 storage, the maximum amount of CO_2 that can be stored and the injectivity of the CO_2 into the reservoir must both be considered (Tsuji et al., 2016). Thus, the results of this study must be combined with information on the effects of M and Ca on the maximum saturation of the nonwetting fluid. In this study, we showed that, for CO_2 as the nonwetting fluid, the relative permeability increases as M increases and decreases as Ca becomes very small. In contrast, Tsuji et al. (2016) demonstrated that the maximum S_{nw} increases as M increases and notably increases at low Ca. Thus, although a high value of M is desirable to increase both the CO_2 capacity and injectivity, a low Ca value can also increase the maximum CO_2 saturation but at the cost of reduced relative permeability. Both factors must be taken into account when choosing suitable conditions for CO_2 storage.

An advantage of using M and Ca is that both parameters are dimensionless, meaning that the results obtained in this pore-scale study can potentially be upscaled to the reservoir scale. Ideally, the pore-scale results are also valid at the reservoir scale as long as the ratios of the parameters (viscosity and IFT) are maintained for both fluids, because the fluid flow behavior at the reservoir scale is controlled by the fluid dynamics at the pore scale. However, this ideal is challenged by the inhomogeneity of the porous medium. The relative permeability is likely to vary throughout the reservoir due to differences in pore size, pore connectivity, and many other factors. Nevertheless, the results of a pore-scale simulation are important to verify relative permeability variations arising from selected factors (in this study, M and Ca) by eliminating other factors. The results of a pore-scale study of relative permeability could then be upscaled by considering the structural factors of the reservoir, e.g., its porosity

and pore connectivity, using advanced techniques such as machine learning.

5 Summary

To evaluate the influence of viscosity ratio M and capillary number Ca on relative permeability k in a two-phase flow system, we calculated k for nonwetting and wetting fluids (k_{nw} and k_w) under various M and Ca conditions using an LBM simulation. The main results of this study are as follows.

1. In our simulations, the relative permeability of the nonwetting fluid increased as the viscosity ratio increased due to the lubricating effect and instability of the fluid interface. Specifically, at high viscosity ratios ($M = 5$), k_{nw} could exceed 1 as a result of the lubricating effect.

2. The relative permeability of the wetting fluid decreased as M increased due to the increase in shear drag force from the nonwetting fluid (viscous coupling effect).

3. As M increased, the Euler number of the nonwetting fluid became higher, indicating that the nonwetting fluid became more disconnected and formed a larger number of clusters. In contrast, the Euler number of the wetting fluid decreased, signifying that the wetting fluid became more connected.

4. At high capillary numbers (log $Ca = 0.75$ to -1.25), k_{nw} did not respond to Ca, but did so at lower values of log Ca (< -1.25) due to the capillary force.

5. As Ca decreased k_w decreased, but at a negligible rate compared to k_{nw}.

6. k_{nw} can change markedly in a wide range of M–Ca parameter space, and the M–Ca–k_{nw} correlation map created in this study can provide k_{nw} estimates at various reservoir conditions.

7. The color map produced from our results is useful for differentiating effects of M and Ca when both apply simultaneously.

Appendices

A. Single-phase simulation

Before conducting the two-phase flow simulations, we first ran single-phase simulations to calculate the absolute permeability of the 3D rock model. Single-phase simulations can also be used to verify the accuracy and precision of the simulation. When only one type of fluid exists in a rock, the absolute permeability can be calculated from Darcy's law:

$$k = \frac{v \ l}{P} \qquad (A.1)$$

where k is the absolute permeability (m^2), v is the average fluid velocity (m/s), is the dynamic viscosity of the fluid (Pa s), Δl is the distance between the inlet and the outlet, and ΔP is the applied pressure difference between the inlet and the outlet. In this study, because the body force was applied only in the z direction, we calculated k in the z direction (k_z).

Because all simulation units are in lattice Boltzmann units, they must subsequently be converted into physical units. The unit conversion for k can be performed using the formula:

$$k_{(\text{physical})} = k_{(LB)} * \ A^2 \qquad (A.2)$$

where A is the resolution of the digital rock, i.e. the physical size of a lattice grid (5.345 µm in this study).

Absolute permeability is an intrinsic property of a rock that is independent of the type of fluid. The single-phase simulations were conducted with several different values of fluid viscosity and body force to ensure the consistency of the results. When the fluid summation of velocity change in 1,000 steps difference was less than 2% for all cases, the simulations were assumed to have converged at that time. The absolute permeability results in various viscosity and body force conditions are shown in the table A.1 below.

kinematic viscosity (lattice-Boltzmann unit)	Body force (lattice-Boltzmann unit)	absolute permeability (Darcy)

The absolute permeability of the Berea rock is 1.760 ±0.001 Darcy. The absolute permeability value remains constant under various conditions, which demonstrates the accuracy and stability of the simulation. The result obtained from this simulation is slightly different from the result by the Dong and Blunt (2009), which gives the absolute permeability value of 1.193 Darcy. The difference might

be due to the difference in size of digital rocks. Dong and Blunt used digital rock with dimension of 400x400x400 voxels (9.77 mm^3 in actual size), while we used digital rock of 320x320x320 voxels (5.00 mm^3 in actual size) is used. The dimension difference might have caused a slight change in the rock sample heterogeneity. In addition, Dong and Blunt applied Pore Network Model (PNM) to calculate the absolute permeability, while in this study, LBM simulation is used. Nonetheless, the absolute permeability value obtained is still in the same order as described by the paper.
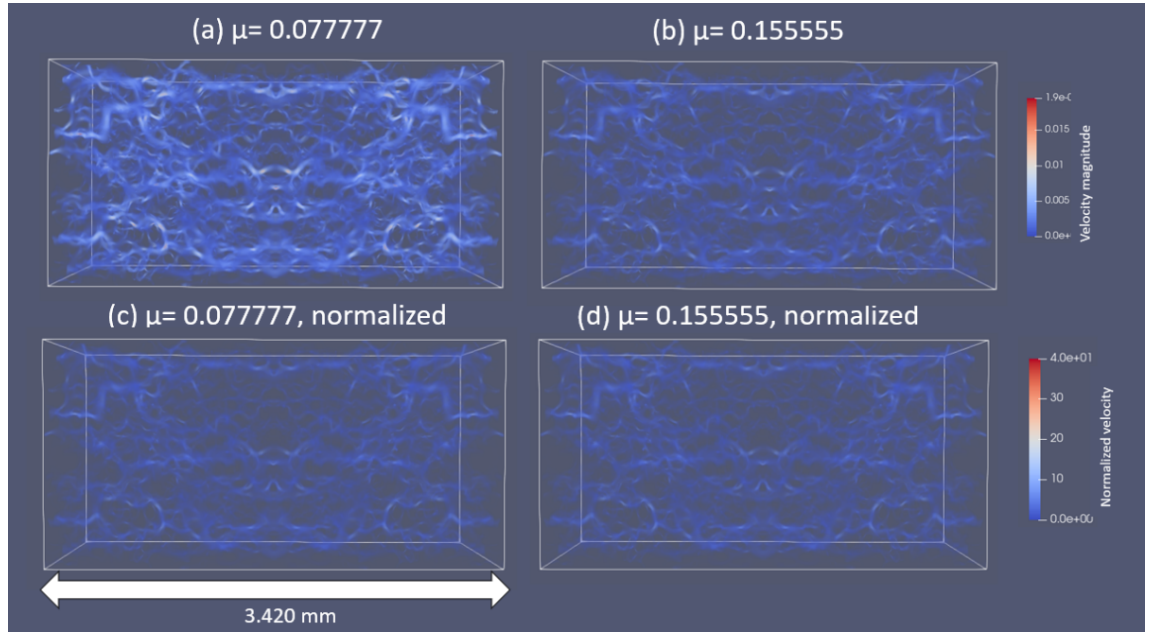
Fig. (A. a) and fig. (A. b) show the velocity field of single-phase simulation for kinematic viscosity = 0.077777 and 0.155555 with equal body force of 0.0001. The fluid velocity for simulation with fluid kinematic viscosity of 0.077777 nu_{LB} is significantly higher compared to the fluid kinematic viscosity of 0.155555 nu_{LB} case. This is because fluid average velocity is inversely proportional to viscosity (equation A.1). Thus, fluid velocity is not proportional to permeability, and must be normalized into dimensionless velocity field. Fig. (A. c) and fig. (A. d) shows the normalized fluid velocity field for both conditions. Both figures show a relatively similar results, which indicate that a similar absolute permeability value is obtained from both conditions.

B. Euler-Poincaré characteristic calculation

We applied Euler-Poincaré characteristic (Euler number) to investigate the fluid connectivity of each fluid phase. Euler-Poincaré characteristic is one of the features in Minkowski measures that describes the topology of the fluid distribution. Euler number measures the connectedness of a fluid phase by counting fluid clusters and inherent loops (Schlüter et al., 2016). In order to apply Minkowski

19

functionals, the image of fluid distributions must be converted into binary structures, where one fluid phase is described as foreground and the other fluid phase and the solid rock is the background. The formula to measure Euler number of a three-dimensional image is as follows:

$$\chi = N \ - \ L + O$$

with χ represents Euler-Poincare characteristic, N is number of individual (unconnected) fluid clusters, L is the number of redundant connections between clusters, and O is the number of isolated background clusters enclosed by foreground clusters. High Euler number indicates the increase of number of unconnected foreground clusters and the decrease of number of isolated background clusters (wetting fluid clusters for nonwetting fluid binary image and nonwetting fluid clusters for wetting fluid binary image). As a 3D Berea digital rock is used as a porous media in this study, the 3D-extended Euler-Poincaré characteristic of the 3D binary nonwetting and wetting fluid images are calculated using the approach proposed by Legland et al. (2007).

References

Ahmadlouydarab, M., Liu, Z. S., & Feng, J. J. (2012). International Journal of Multiphase Flow Relative permeability for two-phase flow through corrugated tubes as model porous media. *International Journal of Multiphase Flow*, *47*, 85–93. http://dx.doi.org/10.1016/j.ijmultiphaseflow.2012.07.005Ahrenholz, B., Tölke, J., Lehmann, P., Peters, A., Kaestner, A., Krafczyk, M., & Durner, W. (2008). Prediction of capillary hysteresis in a porous material using lattice-Boltzmann methods and comparison to experimental data and a morphological pore network model. *Advances in Water Resources*, *31*(9), 1151–1173. https://doi.org/10.1016/j.advwatres.2008.03.009Amaefule, J. O., & Handy, L. L. (1982). The Effect of Interfacial Tensions on Relative Oil/Water Permeabilities of Consolidated Porous Media. *Society of Petroleum Engineers Journal*, *22*(03), 371–381. https://doi.org/10.2118/9783-PAAsar, H., & Handy, L. L. (1989). Influence of interfacial tension on gas/oil relative permeability in a gas-condensate system. *Spe Reservoir Engng.*, *3*(1, Feb. 1989), 257–264. https://doi.org/10.2118/11740-paBenson, S. M., Hingerl, F., Zuo, L., Krevor, S., Reynolds, C., Niu, B., Calvo, R., Niemi, A., Pini, R., Krevor, S., Reynolds, C., Niu, B., Calvo, R., & Niemi, A. (2015). Relative permeability for multiphase flow in CO2 storage reservoirs. Part II: resolving fundamental issues and filling data gaps. *Global CCS Institute*, *December*, 1–52.Burnside, N. M., & Naylor, M. (2014). International Journal of Greenhouse Gas Control Review and implications of relative permeability of CO 2 / brine systems and residual trapping of CO 2. *International Journal of Greenhouse Gas Control*, *23*, 1–11. https://doi.org/10.1016/j.ijggc.2014.01.013Chen, C., & Zhang, D. (2010). Pore-scale simulation of density-driven convection in fractured porous media during geological CO2 sequestration. *Water Resources Research*, *46*(11). https://doi.org/https://doi.org/10.1029/2010WR009453Chen,

S., & Doolen, G. D. (1998). LATTICE BOLTZMANN METHOD FOR FLUID FLOWS. *Annual Review of Fluid Mechanics*, *30*(1), 329–364. https://doi.org/10.1146/annurev.fluid.30.1.329Dong, H., & Blunt, M. J. (2009). Pore-network extraction from micro-computerized-tomography images. *Physical Review E*, *80*(3), 36307. https://doi.org/10.1103/PhysRevE.80.036307Dou, Z., & Zhou, Z. F. (2013). Numerical study of non-uniqueness of the factors influencing relative permeability in heterogeneous porous media by lattice Boltzmann method. *International Journal of Heat and Fluid Flow*, *42*, 23–32. https://doi.org/10.1016/j.ijheatfluidflow.2013.01.020Fan, M., Dalton, L. E., McClure, J., Ripepi, N., Westman, E., Crandall, D., & Chen, C. (2019). Comprehensive study of the interactions between the critical dimensionless numbers associated with multiphase flow in 3D porous media. *Fuel*, *252*, 522–533. https://doi.org/10.1016/j.fuel.2019.04.098Fulcher, R. A., Ertekin, T., & Stahl, C. D. (1985). Effect of Capillary Number and Its Constituents on Two-Phase Relative Permeability Curves. *JPT, Journal of Petroleum Technology*, *37*(2), 249–260. https://doi.org/10.2118/12170-PAGoel, G., Abidoye, L. K., Chahar, B. R., & Das, D. B. (2016). Scale dependency of dynamic relative permeability–satuartion curves in relation with fluid viscosity and dynamic capillary pressure effect. *Environmental Fluid Mechanics*, *16*(5), 945–963. https://doi.org/10.1007/s10652-016-9459-yGoldsmith, H. L., & Mason, S. G. (1963). The flow of suspensions through tubes. II. Single large bubbles. *Journal of Colloid Science*, *18*(3), 237–261. https://doi.org/10.1016/0095-8522(63)90015-1Gudjonsdottir, M., Palsson, H., Eliasson, J., & Saevarsdottir, G. (2015). Calculation of relative permeabilities from field data and comparison to laboratory measurements. *Geothermics*, *54*, 1–9. https://doi.org/10.1016/j.geothermics.2014.10.004Harbert, L. W. (1983). Low interfacial tension relative permeability. *Proceedings - SPE Annual Technical Conference and Exhibition*, *1983-Octob*, 2–9. https://doi.org/10.2523/12171-msHeins, R., Simjoo, M., Zitha, P. L., & Rossen, W. R. (2014). Oil Relative Permeability During Enhanced Oil Recovery by Foam Flooding. In *SPE Annual Technical Conference and Exhibition.* https://doi.org/10.2118/170810-MSHuang, H., & Lu, X. Y. (2009). Relative permeabilities and coupling effects in steady-state gas-liquid flow in porous media: A lattice Boltzmann study. *Physics of Fluids*, *21*(9). https://doi.org/10.1063/1.3225144Huang, H., Sukop, M. C., & Lu, X.-Y. (2015). Rothman–Keller multiphase Lattice Boltzmann model. In *Multiphase Lattice Boltzmann Methods: Theory and Application* (pp. 94–135). https://doi.org/https://doi.org/10.1002/9781118971451.ch4Huang, H., Wang, L., & Lu, X. Y. (2011). Evaluation of three lattice Boltzmann models for multiphase flows in porous media. *Computers and Mathematics with Applications*, *61*(12), 3606–3617. https://doi.org/10.1016/j.camwa.2010.06.034Jeong, G. S., Lee, J., Ki, S., Huh, D. G., & Park, C. H. (2017). Effects of viscosity ratio, interfacial tension and flow rate on hysteric relative permeability of CO2/brine systems. *Energy*, *133*, 62–69. https://doi.org/10.1016/j.energy.2017.05.138Jiang, F., & Tsuji, T. (2015). Impact of interfacial tension on residual CO2 clusters in porous sandstone. *Water Resources Research*, *51*(3), 1710–1722.

https://doi.org/10.1002/2014WR016070Jiang, F., & Tsuji, T. (2016). Numerical investigations on the effect of initial state CO2 topology on capillary trapping efficiency. *International Journal of Greenhouse Gas Control*, *49*, 179–191. https://doi.org/10.1016/j.ijggc.2016.03.006Jiang, F., Tsuji, T., & Hu, C. (2014). Elucidating the Role of Interfacial Tension for Hydrological Properties of Two-Phase Flow in Natural Sandstone by an Improved Lattice Boltzmann Method. *Transport in Porous Media*, *104*(1), 205–229. https://doi.org/10.1007/s11242-014-0329-0Legland, D., Kiêu, K., & Devaux, M. F. (2007). Computation of Minkowski measures on 2D and 3D binary images. *Image Analysis and Stereology*, *26*(2), 83–92. https://doi.org/10.5566/ias.v26.p83-92Lenormand, R., Touboul, E., & Zarcone, C. (1988). Numerical models and experiments on immiscible displacements in porous media. *Journal of Fluid Mechanics*, *189*, 165–187. https://doi.org/10.1017/S0022112088000953Li, H., Pan, C., & Miller, C. T. (2005). Pore-scale investigation of viscous coupling effects for two-phase flow in porous media. *Physical Review E - Statistical, Nonlinear, and Soft Matter Physics*, *72*(2), 1–14. https://doi.org/10.1103/PhysRevE.72.026705Mahmoudi, S., Mohammadzadeh, O., Hashemi, A., & Kord, S. (2017). Pore-scale numerical modeling of relative permeability curves for CO2–oil fluid system with an application in immiscible CO2 flooding. *Journal of Petroleum Exploration and Production Technology*, *7*(1), 235–249. https://doi.org/10.1007/s13202-016-0256-4McDougall, S. R., Salino, P. A., & Sorbie, K. S. (2007). *The Effect of Interfacial Tension Upon Gas-Oil Relative Permeability Measurements: Interpretation Using Pore-Scale Models.* https://doi.org/10.2523/38920-msNiibori, Y., Ahn, J., & Mimura, H. (2011). Uncertainty of Relative Permeability to Describe Two-Phase Flow in Geological Disposal System. *Nuclear Technology*, *175*(3), 641–651. https://doi.org/10.13182/NT11-A12512Odeh, A. S. (1959). Effect of Viscosity Ratio on Relative Permeability (includes associated paper 1496-G). *Transactions of the AIME*, *216*(01), 346–353. https://doi.org/10.2118/1189-GØren, P. E., & Bakke, S. (2003). Reconstruction of Berea sandstone and pore-scale modelling of wettability effects. *Journal of Petroleum Science and Engineering*, *39*(3–4), 177–199. https://doi.org/10.1016/S0920-4105(03)00062-7Ramstad, T., Øren, P. E., & Bakke, S. (2010). Simulation of two-phase flow in Reservoir rocks using a lattice Boltzmann method. *SPE Journal*, *15*(4), 923–933. https://doi.org/10.2118/124617-paSchlüter, S., Berg, S., Rücker, M., Armstrong, R. T., Vogel, H.-J., Hilfer, R., & Wildenschild, D. (2016). Pore-scale displacement mechanisms as a source of hysteresis for two-phase flow in porous media. *Water Resources Research*, *52*, 2194–2005. https://doi.org/10.1002/2015WR018254Shad, S., Gates, I. D., & Maini, B. B. (2008). Experimental study of heavy oil-water flow structure effects on relative permeabilities in a fracture filled with heavy oil. *Society of Petroleum Engineers - International Thermal Operations and Heavy Oil Symposium, ITOHOS 2008 - "Heavy Oil: Integrating the Pieces," 2*, 690–701. https://doi.org/10.2118/117644-msShen, P., Zhu, B., Li, X. Bin, & Wu, Y. S. (2010). An Experimental Study of the Influence of Interfacial Tension onWater-Oil Two-Phase Relative Permeability. *Transport in Porous Media*, *85*(2), 505–520. https://doi.org/10.1007/s11242-010-9575-ySucci, S., Sbra-

gaglia, M., & Ubertini, S. (2010). Lattice Boltzmann Method. *Scholarpedia*, *5*(5), 9507. https://doi.org/10.4249/scholarpedia.9507Tölke, J., Freudiger, S., & Krafczyk, M. (2006). An adaptive scheme using hierarchical grids for lattice Boltzmann multi-phase flow simulations. *Computers & Fluids*, *35*(8), 820–830. https://doi.org/https://doi.org/10.1016/j.compfluid.2005.08.010Tsuji, T., Jiang, F., & Christensen, K. T. (2016). Characterization of immiscible fluid displacement processes with various capillary numbers and viscosity ratios in 3D natural sandstone. *Advances in Water Resources*, *95*, 3–15. https://doi.org/10.1016/j.advwatres.2016.03.005Vafai, K. (2000). *Handbook of Porous Media*. Marcel Dekker, Inc.Wu, Q., & Wang, J. (2020). A thermo-hydro-mechanical coupling analysis for the contaminant transport in a bentonite barrier with variable saturation. *Water (Switzerland)*, *12*(11), 1–23. https://doi.org/10.3390/w12113114Yang, J., & Boek, E. S. (2013). A comparison study of multi-component Lattice Boltzmann models for flow in porous media applications. *Computers and Mathematics with Applications*, *65*(6), 882–890. https://doi.org/10.1016/j.camwa.2012.11.022Yiantsios, S. G., & Higgins, B. G. (1988). Numerical solution of eigenvalue problems using the compound matrix method. *Journal of Computational Physics*, *74*(1), 25–40. https://doi.org/10.1016/0021-9991(88)90066-6Yih, C. S. (1967). Instability due to viscosity stratification. *Journal of Fluid Mechanics*, *27*(2), 337–352. https://doi.org/10.1017/S0022112067000357Yiotis, A. G., Psihogios, J., Kainourgiakis, M. E., Papaioannou, A., & Stubos, A. K. (2007). A lattice Boltzmann study of viscous coupling effects in immiscible two-phase flow in porous media. *Colloids and Surfaces A: Physicochemical and Engineering Aspects*, *300*(1-2 SPEC. ISS.), 35–49. https://doi.org/10.1016/j.colsurfa.2006.12.045Zhang, Y., Jiang, F., & Tsuji, T. (2022). Influence of pore space heterogeneity on mineral dissolution and permeability evolution investigated using lattice Boltzmann method. *Chemical Engineering Science*, *247*, 117048. https://doi.org/10.1016/j.ces.2021.117048Zhao, H., Ning, Z., Kang, Q., Chen, L., & Zhao, T. (2017). Relative permeability of two immiscible fluids flowing through porous media determined by lattice Boltzmann method. *International Communications in Heat and Mass Transfer*, *85*(May), 53–61. https://doi.org/10.1016/j.icheatmasstransfer.2017.04.020Zheng, X., Mahabadi, N., Yun, T. S., & Jang, J. (2017). Effect of capillary and viscous force on CO2 saturation and invasion pattern in the microfluidic chip. *Journal of Geophysical Research: Solid Earth*, *122*(3), 1634–1647. https://doi.org/https://doi.org/10.1002/2016JB013908